Supplementary Information

Construct mesoporous MXenes by thermal shock induced pore engineering for high performance supercapacitor

Xiaolong Lu,[a,b] Cancan Li,[a] Ziyi Chen,[a] Ben Zhou,[a,c] Can Tu,[a] Bijun Fang,[a] Ningyi Yuan,[*a] Chao Huangfu[*c]

a School of Materials Science and Engineering, Jiangsu Collaborative Innovation Center for Photovoltaic Science and Engineering, Changzhou University, Changzhou, 213164, China. Email: nyyuan@cczu.edu.cn
b Key Laboratory of Multi-spectral Absorbing Materials and Structures, Ministry of Education, University of Electronic Science and Technology of China, Chengdu, 611731, China.
c Collage of Automotive Engineering, Changzhou Institute of Technology, Changzhou, 213032, China. Email: huangfc@czu.cn.

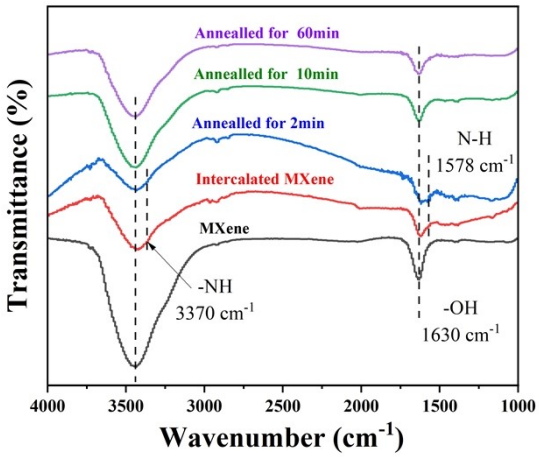

Fig. S1 FITR spectra of multilayer MXene, intercalated MXene and annealed MXene samples.

To affirm the interaction between n-butylamine and MXenes, Fourier transform infrared spectroscopy (FTIR) detection was performed. And then, during rapid annealing, to optimize the time of annealing and check the possible structure evolution, various times of 2, 10, 60 min were adopted. It is observed that when the annealing duration is maintained at 2 min, residual n-butylamine molecules remained within the MXene interlayers. However, for annealing times extended to 10 and 60 minutes, no detectable N-H vibrational signal is observed in the spectroscopic analysis, while the characteristic -OH peak shifts back to 1630 cm^{-1}, indicating the complete elimination of n-butylamine.

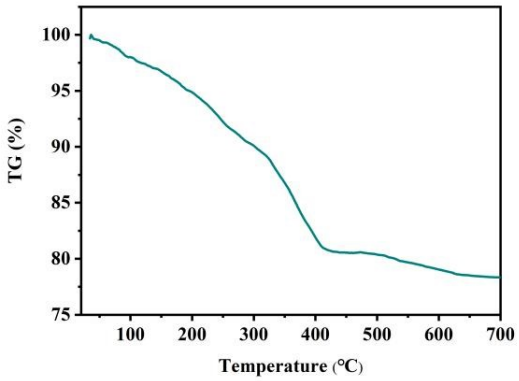

Fig. S2 The TG curve of intercalated MXenes.

The boiling point of $C_4H_{11}N$ is about 78 ℃. Obvious weight loss under 450 ℃ could be found and are ascribed to the evaporation and pyrolysis of intercalated $C_4H_{11}N$ and surface functional groups of MXenes. To guarantee the remove of $C_4H_{11}N$, the annealing temperature was set at 500 ℃.

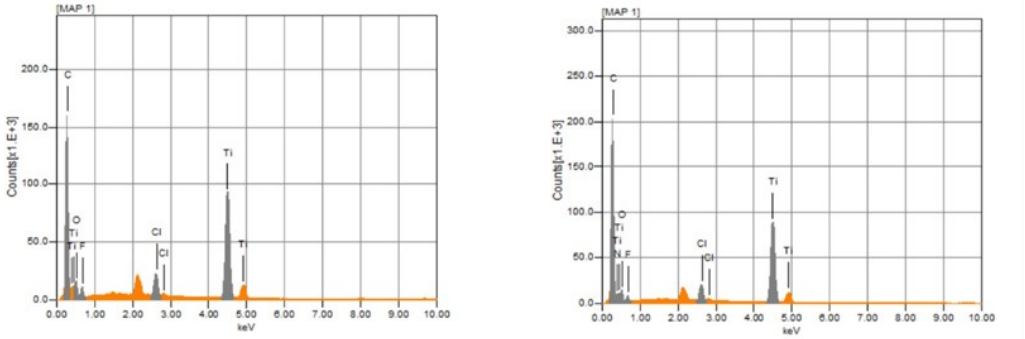

Formula	mass%	Atom%	Sigma	Net	K ratio	Line
C	41.14	65.34	0.00	3287540	0.2942141	K
O	10.45	12.46	0.02	336985	0.0988376	K
F	4.09	4.11	0.01	226076	0.1283238	K
Cl	3.18	1.71	0.01	953184	0.2241134	K
Ti	41.14	16.38	0.02	5482641	2.6357641	K
Total	100.00	100.00				

Formula	mass%	Atom%	Sigma	Net	K ratio	Line
C	46.40	70.41	0.00	4011682	0.3590203	K
O	9.38	10.69	0.02	302633	0.0887622	K
F	2.94	2.82	0.01	164480	0.0933614	K
Cl	2.81	1.44	0.00	868301	0.2041556	K
Ti	38.48	14.64	0.02	5275826	2.5363381	K
Total	100.00	100.00				

Fig. S3 EDS element analysis of multilayer MXenes (left) and annealed MXenes (right).

The existance and decrease of F, O and Cl elements confirm, to a certain degree, the partial remove and residual of surface functional groups after rapid annealing, although the EDS analysis is non-quantitative.

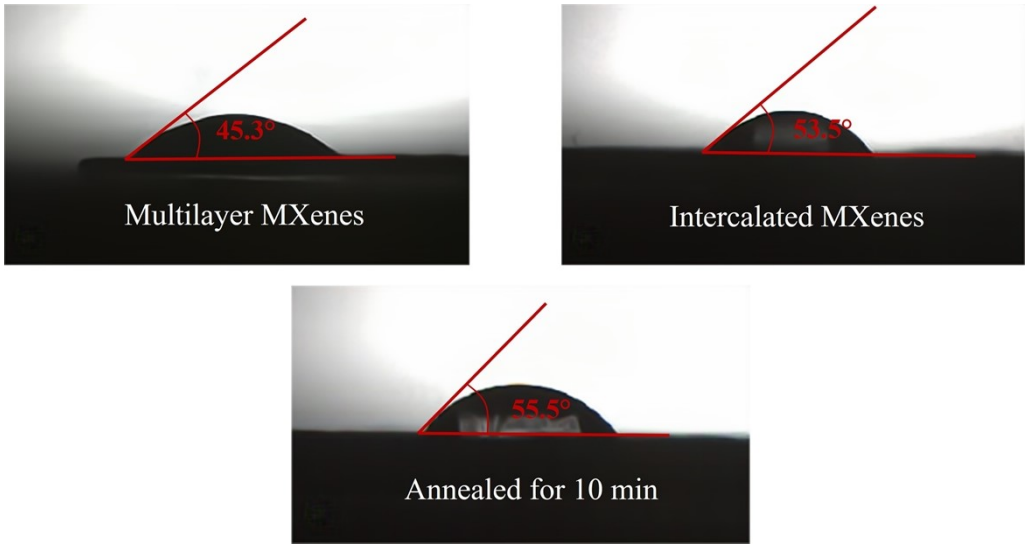

Fig. S4 The contact angle tests of the powders of multilayer MXenes, intercalated MXenes and annealed MXenes for 10 min.

The contact angle tests of the powders of multilayer MXene, intercalated MXene and annealed MXene for 10 min were conducted. It can be observed that multilayer MXenes show hydrophility due to their surface functional groups. After intercalation, the contact angle between the MXenes and the water droplets increased from 45.3° to 53.5°, indicating a slight decrease for the hydrophilicity. This can be attributed to the hydrophilic end -NH_2 of n-butylamine forming hydrogen bonds with the functional

groups of MXenes as showed in FTIR spectroscopy, while the hydrophobic end -C_4H_9 covers the surface of MXenes.[1] After rapid annealing for 10 min, the intercalated n-butylamine is sublimated and pyrolyzed due to thermal shock, and partial functional groups are removed. The annealed MXenes still show hydrophilicity, although the contact angle gets increased. This could be derived from the residual functional groups because of the short treatment process of rapid annealing and open-up framework of annealed MXenes due to the microexplosion effect (Fig. 2f). The hydrophilic annealed MXenes are advantageous for further exfoliation and preparation of M-MXenes.

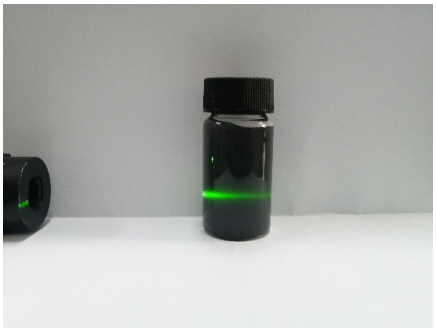

Fig. S5 The optical image showing the Tyndall effect of dispersed M-MXene nanosheets.

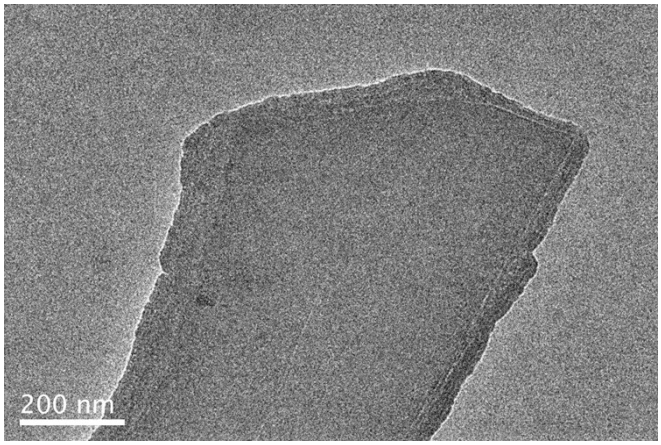

Fig. S6 TEM images of obtained D-MXene nanosheets.

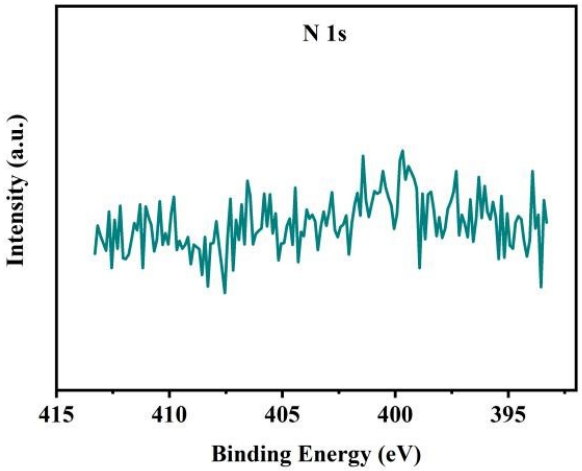

Fig. S7 XPS spectrum of N element in annealed MXenes.

Table. S1 Detailed XPS peak fitting results of Ti and O spectra.

Rapid annealed sample:

Region	BE (eV)	Fraction (%)	Assigned to
Ti 2P3/2 (2p1/2)	454.5/460.3	23.5	Ti-C
	455.2/460.8	24.6	Ti (Ⅱ)
	456.3/462	32.4	Ti (Ⅲ)
	458.3/464	11.9	Ti-O
	459/465.1	7.6	Ti-F

Region	BE (eV)	Fraction (%)	Assigned to
O 1s	530.4	32.01	TiO_2
	531.2	21.35	C-Ti-O_x
	533.0	41.26	C-Ti-$(OH)_x$
	534.8	5.38	H_2O

Unannealed sample:

Region	BE (eV)	Fraction (%)	Assigned to
Ti 2P3/2 (2p1/2)	454.5/460.3	27.2	Ti-C
	455.2/460.8	24.2	Ti (Ⅱ)
	456.3/462	33.2	Ti (Ⅲ)
	458.1/464	6.5	Ti-O
	458.7/465.1	8.9	Ti-F

Region	BE (eV)	Fraction (%)	Assigned to
O 1s	530.3	13.64	TiO_2
	531.2	8.32	C-Ti-O_x
	533.1	63.99	C-Ti-$(OH)_x$
	534.8	14.05	H_2O

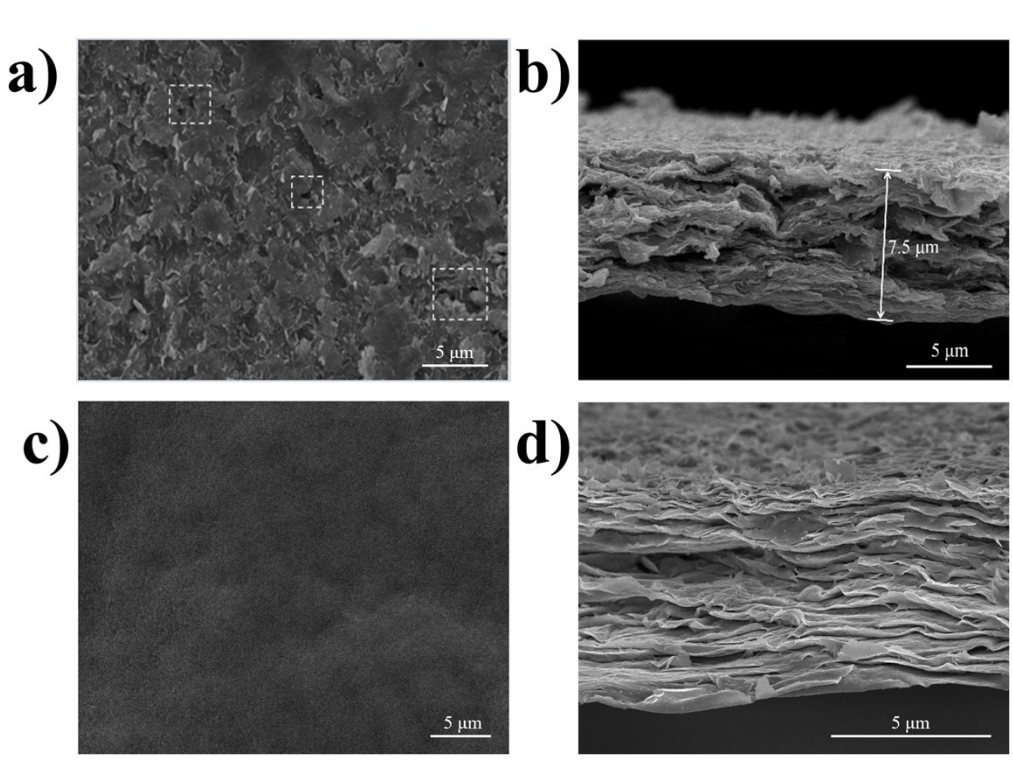

Fig. S8 The SEM images of filtered M-MXene film and D-MXene film. a) Surface and b) Cross section morphologies of M-MXene film. c) Surface and d) Cross section morphologies of D-MXene film.

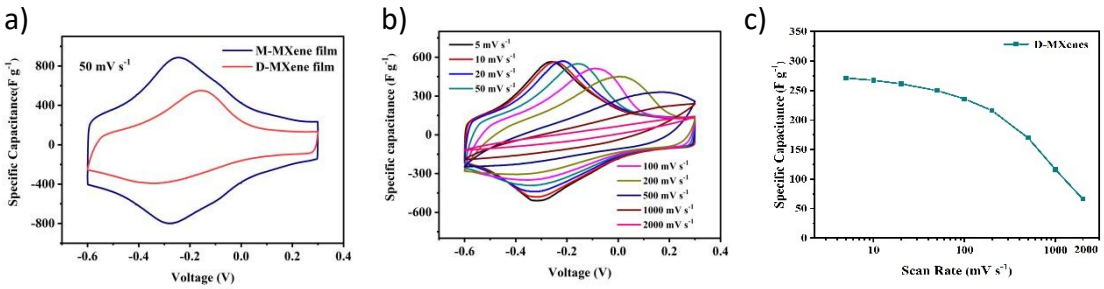

Fig. S9 a) Comparison of CV curves of M-MXene and D-MXene electrodes at 50 mV s^{-1}; b) The CV curves of D-MXene electrode at different scan rates; c) The specific capacitance of D-MXenes at different scan rates.

Table S2 Comparison of the specific capacitance and rate performance.

Num-ber	Materials	Synthesis route	Electrolyte	Potential	Capacitan-ce	Rate Capability	Ref
1	3D porous $Ti_3C_2T_x$ films	freeze-casting assembly	3 M H_2SO_4	-0.5~0.3 V	358.8 F g^{-1} (20 mV s^{-1})	58.6% (10 V s^{-1})	[2]
2	MXene hydrogel	metal ions induced gelation	3 M H_2SO_4	-1.1~-0.15 V	272 F g^{-1} (2 mV s^{-1})	83.1% (1 V s^{-1})	[3]
3	3D $Ti_3C_2T_x$/ CNTs film	in situ ice template strategy	3 M H_2SO_4	-0.7~0.3 V	375 F g^{-1} (5 mV s^{-1})	67% (1000 mV s^{-1})	[4]
4	$Ti_3C_2T_x$-RGO film	microscopic explosion of GO	3 M H_2SO_4	-0.6~0.3V	505 F g^{-1} (2 mV s^{-1})	69.9% (100 mV s^{-1})	[5]
5	3D $Ti_3C_2T_x$ aerogels	thermal treatment at a mild temperature	3 M H_2SO_4	-0.6~0.2 V	438 F g^{-1} (10 mV s^{-1})	79.7% (2000 mV s^{-1})	[6]
6	Compact nanoporous MXene film	freeze-drying and mechanically pressing	3 M H_2SO_4	-0.5~0.3V	345 F g^{-1} (2 mV s^{-1})	50% (500 mV s^{-1})	[7]
7	MXene-rGO	self-propagation	3 M H_2SO_4	-0.6~0.2 V	329.2 F g^{-1} (20 mV s^{-1})	78.8% (1000 mV s^{-1})	[8]
8	3D macroporous $Ti_3C_2T_x$	mild gelation	3 M H_2SO_4	-0.6~0.25 V	349 F g^{-1} (2 mV s^{-1})	57.9% (2 V s^{-1})	[9]
9	MXene/rGO 3D porous aerogel	dual utilization strategy of lignosulfonate	3 M H_2SO_4	-0.55~0.2V	386 F g^{-1} (2 mV s^{-1})	62.5% (100 mV s^{-1})	[10]
10	Macroporous $Ti_3C_2T_x$ film	PMMA spheres sacrificial template	3 M H_2SO_4	-1.1~-0.1V	450 F g^{-1} (10 mV s^{-1})	46.7% (10 V s^{-1})	[11]
11	Porous Ti_3C2T_x film	H_2SO_4 oxidation	3 M H_2SO_4	-1.2~-0.2V	324 F g^{-1} (5mV s^{-1})	64% (10 V s^{-1})	[12]

12	3D porous MXene/graphene	in situ sacrificial metallic zinc template	3 M H_2SO_4 + 50 mM LiBr	-0.6~-0.25V	393 F g^{-1} (2mV s^{-1})	32.7% (10 V s^{-1})	[13]
13	PANI/MXene film	blade coating	1 M H_2SO_4	-0.2~-0.8V	560 F g^{-1} (5mV s^{-1})	64% (100 mV s^{-1})	[14]
14	$Ti_3C_2T_x/Nb_2CT_x$ film	vacuum-assisted filtration	2 M H_2SO	-0.8~-0.1 V	370 F g^{-1} (2 mV/s)	56.1% (200 mV s^{-1})	[15]
15	N-$Ti_3C_2T_x$ film	electrostatic adsorption and calcination	3 M H_2SO_4	-1.1~-0.4V	415 F g^{-1} (2 mV s^{-1})	75.9% (200 mV s^{-1})	[16]
16	MXene/rHGO	filtration and annealing treatment	3 M H_2SO_4	-0.7~0.3 V	438 F g^{-1} (2 mV s^{-1})	69% (500 mV s^{-1})	[17]
17	MXene/graphene	metallic zinc particles induced gelation	3 M H_2SO_4	-0.7~0.3 V	357 F g^{-1} (10 mV s^{-1})	60% (500 mV s^{-1})	[18]
18	MXene/PANI	self-assembly	1 M H_2SO_4	-0.65~0.2V	377 F g^{-1} (2 mV s^{-1})	33% (200 mV s^{-1})	[19]
19	dodecaborate/ MXene composites	electrostatic adsorption	1 M H_2SO_4	-0.2~0.35V	366 F g^{-1} (2 mV s^{-1})	58.2% (200 mV s^{-1})	[20]
20	MXene/rGO	electrostatic self-assembly	3 M H_2SO_4	-0.7~0.3 V	335 F g^{-1} (2 mV s^{-1})	48.9% (3000 mV s^{-1})	[21]
21	Mesoporous gold/$Ti_3C_2T_x$ film	vacuum-assisted filtration	3 M H_2SO_4	-0.8~-0.2 V	268 F g^{-1} (2 mV s^{-1})	81.3% (20 mV s^{-1})	[22]
22	3D porous $Ti_3C_2T_x$ aerogel	H_2O_2 oxidation, Zn reduction and freeze-drying	3 M H_2SO_4	-0.6~0.2 V	379 F g^{-1} (2 mV s^{-1})	76.7% (1 V s^{-1})	[23]
23	MXene/C_{PAQ}	vacuum-assisted filtration and calcination	3 M H_2SO_4	-0.6~0.3 V	556 F g^{-1} (2 mV s^{-1})	49.4% (1 V s^{-1})	[24]
24	3D porous $Ti_3C_2T_x$ aerogel	$FeCl_3$ oxidation and freeze-drying	3 M H_2SO_4	-1.0~-0.1 V	304 F g^{-1} (10 mV s^{-1})	79.0% (1 V s^{-1})	[25]
25	MXene/MHCS/CNT film	vacuum-assisted filtration	3 M H_2SO_4	-0.6~0.3 V	395 F g^{-1} (2 mV s^{-1})	70.9% (1 V s^{-1})	[26]
26	3D porous $Ti_3C_2T_x$	zinc-assisted electrodeposition and freeze-drying	3 M H_2SO_4	-0.6~0.2 V	352 F g^{-1} (2 mV s^{-1})	73.3% (1 V s^{-1})	[27]

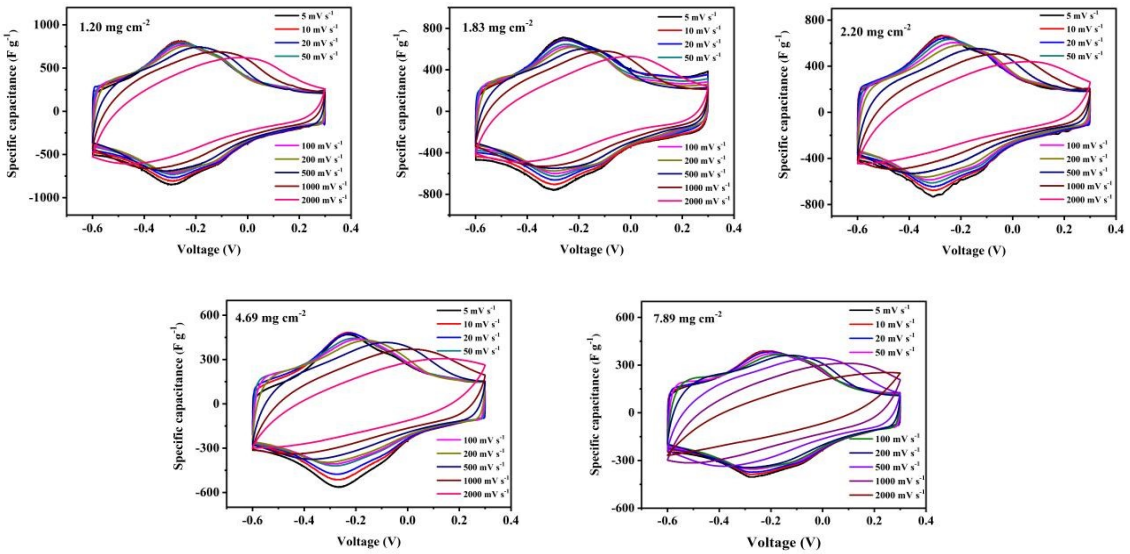

Fig. S10 The CV curves of M-MXene electrodes at different scan rates with different loading masses.

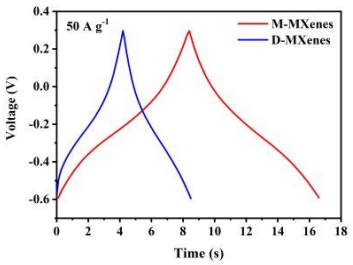

Fig. S11 The GCD curves of M-MXene and D-MXene electrodes at a current density of 50 A g^{-1}.

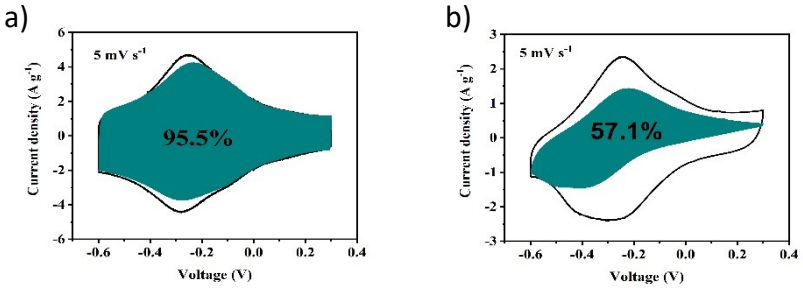

Fig. S12 The capacitive-controlled contribution for M-MXenes a) and D-MXenes b) at scan rate 5 mV s^{-1}.

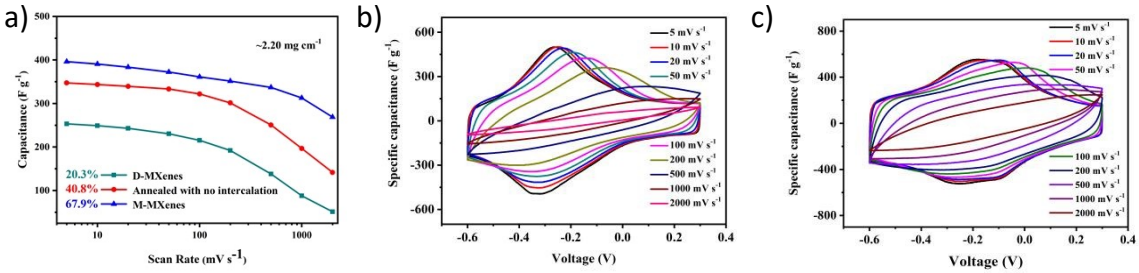

Fig. S13 Comparison of the D-MXenes, annealed MXenes with no intercalation and M-MXenes with a mass loading of ~2.20 mg cm^{-2} at different scan rates; a) Their specific capacitance at different scan rates; b) CV curves of D-MXenes; c) CV curves of annealed MXenes with no intercalation.

Reference

1 C. Zhou, D. Wang, F. Lagunas, B. Atterberry, M. Lei, H. Hu, Z. Zhou, A. S. Filatov, D. Jiang, A. J. Rossini, R. F. Klie and D. V. Talapin, Nat. Chem., 2023, **15**, 1722-1729.

2 J. Kong, H. Yang, X. Guo, S. Yang, Z. Huang, X. Lu, Z. Bo, J. Yan, K. Cen, and K. K. Ostrikov, ACS Energy Lett., 2020, **5**, 2266-2274.

3 Y. Deng, T. Shang, Z. Wu, Y. Tao, C. Luo, J. Liang, D. Han, R. Lyu, C. Qi, W. Lv, F. Kang and Q. H. Yang, Adv. Mater., 2019, **31**, 1902432.

4 P. Zhang, Q. Zhu, R. A. Soomro, S. He, N. Sun, N. Qiao, and B. Xu, Adv. Funct. Mater., 2020, **30**, 2000922.

5 Y. Fang, B. Yang, D. He, H. Li, K. Zhu, L. Wu, K. Ye, K. Cheng, J. Yan, G. Wang and D. Cao, Chin. Chem. Lett., 2020, **31**, 1004-1008.

6 X. Wang, Q. Fu, J. Wen, X. Ma, C. Zhu, X. Zhang, and D. Qi, Nanoscale, 2018, **10**, 20828-20835.

7 Z. Fan, J. Wang, H. Kang, Y. Wang, Z. Xie, Z. Cheng, and Y. Liu, ACS Appl. Energy Mater., 2020, **3**, 1811-1820.

8 J. Miao, Q. Zhu, K. Li, P. Zhang, Q. Zhao, and B. Xu, J. Energy Chem., 2021, **52**, 243-250.

9 X. Yang, Y. Yao, Q. Wang, K. Zhu, K. Ye, G. Wang, D. Cao and J. Yan, Adv. Funct. Mater., 2022, **32**, 2109479.

10 L. Ma, T. Zhao, F. Xu, T. You, and X. Zhang, Chem. Eng. J., 2021, **405**, 126694.

11 M. R. Lukatskaya, S. Kota, Z. Lin, M.-Q. Zhao, N. Shpigel, M. D. Levi, J. Halim, P.-L. Taberna, M. W. Barsoum, P. Simon and Y. Gogotsi, Nat. Energy, 2017, **2**, 17105.

12 J. Tang, T. Mathis, X. Zhong, X. Xiao, H. Wang, M. Anayee, F. Pan, B. Xu and Y. Gogotsi, Adv. Energy Mater., 2021, **11**, 2003025.

13 X. Yang, Q. Wang, K. Zhu, K. Ye, G. Wang, D. Cao, and J. Yan, Adv. Funct. Mater., 2021, **31**, 2101087.

14 Y. Wang, X. Wang, X. Li, Y. Bai, H. Xiao, Y. Liu, and G. Yuan, Chem. Eng. J. 2021, **405**, 126664.

15 Z. Li, Y. Dall'Agnese, J. Guo, H. Huang, X. Liang, and S. Xu, J. Mater. Chem. A, 2020, **8**, 16649-16660.

16 Y. Tian, W. Que, Y. Luo, C. Yang, X. Yin, and L. B. Kong, J. Mater. Chem. A, 2019, **7**, 5416-5425.

17 Z. Fan, Y. Wang, Z. Xie, D. Wang, Y. Yuan, H. Kang, B. Su, Z. Cheng and Y. Liu, Adv. Sci., 2018, **5**, 1800750.

18 A. Sikdar, P. Dutta, S. K. Deb, A. Majumdar, N. Padma, S. Ghosh, and U. N. Maiti, Electrochimica Acta, 2021, **391**, 138959.

19 X. Wang, Y. Wang, D. Liu, X. Li, H. Xiao, Y. Ma, M. Xu, G. Yuan and G. Chen, ACS Appl. Mater. Interfaces, 2021, **13**, 30633-30642.

20 Z. Li, C. Ma, Y. Wen, Wei, Z. X. Xing, J. Chu, C. Yu, K. Wang and Z. K. Wang, Nano Res., 2020, **13**, 196-202.

21 J. Yan, C. E. Ren, K. Maleski, C. B. Hatter, B. Anasori, P. Urbankowski, A. Sarycheva and Y. Gogotsi, Adv. Funct. Mater., 2017, **27**, 1701264.

22 Y. Luo, W. Que, A. S. Nugraha, Y. Kang, Y. Tang, Z. Wu, J. Henzie, and Y. Yamauchi, J. Mater. Chem. A, 2025, **13**, 1330-1342.

23 P. Ji, L. Liu, Y. Deng, Y. Luo, Y. Cao, B. Li, K. Wu, X. Dong, Z. Liu and Y. Tai, J. Energy Storage, 2024, **93**, 112194.

24 R. Ma, L. Cao, J. Zhuo, J. Lu, J. Chen, J. Huang, G. Yang and F. Yi, Adv. Energy Mater., 2023, **13**, 2301219.

25 W. Yan, S. Yan, D. Cai, Z. Tian, L. Guo, and Y. Wang, Electrochimica Acta, 2025, **532**, 146479.

26 F. Yang, K. Lv, X. Zhao, D. Kong, N. Kong, Z. Luo, J. Tao, J. Zhou, J. M. Razal and J. Zhang, Chem. Eng. J., 2024, **494**, 153246.

27 P. Ji, W. Chen, Y. Luo, Y. Wang, N. Gu, G. Meng, J. Wu, B. Li, K. Wu and Z. Liu, J. Alloy. Compd., 2024, **997**, 174426.